











# Color Correction and Naturalness Restoration for Multiple Images With Uneven Luminance

Changyou Xu , Zhonghua Hong , *Member, IEEE*, Xiaohua Tong , *Senior Member, IEEE*, Shijie Liu , *Member, IEEE*, Ruyan Zhou , Haiyan Pan , Yun Zhang , Yanling Han , Jing Wang , and Shuhu Yang 

**Abstract**—When multiple synthetic aperture radar images are stitched together, the intensity disconnects between them can have a significant impact on the mosaic’s quality. Many approaches focus on decreasing the intensity differences between images while ignoring the issue of image quality improvement. This study provides an algorithm for color correction and naturalness restoration for multiple images with uneven luminance in order to generate high-quality mosaics. To increase the illuminance component’s naturalness, the image is first divided into illuminance and reflectance components, and the illuminance component is subjected to adaptive luminance improvement and contrast enhancement. Using a color consistency optimization approach, the intensity disparities between illuminance components are subsequently minimized. The reflectance and enhanced illuminance components are then combined to produce an improved image. After that, the enhanced image is mosaicked using multiband blending. Finally, the intensity differences between the enhanced images are further decreased using the block-based Wallis transform based on the mosaic. We assessed the proposed method on 402 Sentinel-1 images covering the majority of China’s land area to verify its robustness. When compared to similar algorithms, our strategy reduces the color distance by about 36.72%, improves the average gradient by around 89.44%, and increases the patch-based contrast quality index by roughly 32.85%. The experimental outcomes reveal that our approach has considerable advantages in terms of color correction and image quality improvement, both visually and quantitatively.

**Index Terms**—Color correction, naturalness restoration, remote sensing images, Retinex theory.

## I. INTRODUCTION

SYNTHETIC aperture radar (SAR) is useful in areas such as environmental monitoring, resource exploration, and disaster assessment, as it is weather-independent and enables all-weather Earth observation [1], [2], [3], [4], [5]. Due to the

Manuscript received 6 January 2024; revised 28 February 2024; accepted 19 March 2024. Date of publication 25 March 2024; date of current version 3 April 2024. This work was supported by the National Natural Science Foundation of China under Grant 42221002 and Grant 42241164. (*Corresponding author: Zhonghua Hong.*)

Changyou Xu, Zhonghua Hong, Ruyan Zhou, Haiyan Pan, Yun Zhang, Yanling Han, Jing Wang, and Shuhu Yang are with the College of Information Technology, Shanghai Ocean University, Shanghai 201306, China (e-mail: m210901453@st.shou.edu.cn; zhong@shou.edu.cn; ryzhou@shou.edu.cn; hy-pan@shou.edu.cn; y-zhang@shou.edu.cn; ylhan@shou.edu.cn; wangjing@shou.edu.cn; shyang@shou.edu.cn).

Xiaohua Tong and Shijie Liu are with the College of Surveying and Geo-Informatics, Tongji University, Shanghai 200092, China (e-mail: xhtong@tongji.edu.cn; liusjtj@tongji.edu.cn).

Digital Object Identifier 10.1109/JSTARS.2024.3380602

limitations of a single image’s coverage, it is frequently required to smoothly composite multiple images into a mosaic when analyzing and studying SAR data on a wide scale. Seasonal variations, radar wave signal attenuation, noise, and different gain mistakes, on the other hand, can produce large intensity variances across images [6]. The radiometric discrepancy lowers the visual quality of the mosaic images significantly. Thus, in the fields of large-scale mapping and environmental monitoring, offering an algorithm to minimize intensity discrepancies between images so that imagery taken at different periods or locations has consistent intensity after stitching is critical. The majority of the approaches used for radiative normalization of SAR images are taken from techniques used for optical image normalization. As a result, it is necessary to review the strategies for radiative normalization of optical images.

Radiometric normalization approaches are categorized as global, local, or combination models [7]. Global models suppose that the radiometric mapping relationship among image pairs can be fitted using a linear or nonlinear function. Such methods are further classified as pixel-to-pixel and area-to-area. To determine the radiometric mapping relationship between images, the pixel-to-pixel method is based on the intensity values of homonymous image points. The relationship between inter-image radiance mapping is typically considered to be linear when there is no change in the features in the overlapping portions of the images. Two popular techniques in this situation are those based on linear regression [8] and least-mean-square transformation. We will determine the nonlinear relationship between neighboring images [9], [10], [11] and then carry out the radiometric normalization when the intensity values of the chosen homonymous image points do not satisfy the linear relationship. The quality of the acquired homonymous image points, however, determines how effective these techniques are.

When images are not exactly aligned or include feature differences in the overlapping areas, region-to-region approaches perform better than pixel-to-pixel techniques. This is because the statistical data in the overlapping areas is used by these methods to determine the radiometric mapping relationship between images. Histogram-based [12], [13], [14], [15] and mean- and variance-based [16], [17], [18] strategies are examples of representative techniques. While the former can process images with similar features well when the radiometric features fluctuate greatly between images, there is a chance that the image texture will be destroyed by altering the image’s mean and variance.

When processing images with similar histogram shapes, the latter can produce better results; nevertheless, there is a risk of altering the local radiometric properties of the images when the histogram shapes differ significantly. To sum up, since the area-to-area approach builds the radiometric mapping association using the statistical data of the overlapped areas, it is not affected by the alignment precision. Overall, a consistent tone can be satisfactorily obtained with the region-to-region methodology.

When the image has high spatial resolution and complex content, global models that change the radiometric features of the entire image using radiometric mapping of overlapping regions frequently disregard local radiometric variances. As a result, some local models that take into account local radiometric changes have been presented [19], [20], [21], [22]. The key idea behind the local model is to create an appropriate normalization function based on the radiance difference of local features. Local models, as a beneficial supplement to global models, can successfully handle the problem of local inconsistency of intensity. However, if processing patterns and levels do not match the local features, local models can result in new radiometric discrepancies. Some scholars have put forward a combination model that integrates the advantages of the two types of models mentioned above [23], [24], [25]. The local model is then used to further minimize the local intensity discrepancies after the global model has been used to reduce the global color inconsistency. To sum up, the local model uses multiple local functions to remove the intensity disparities in the overlapping regions, whereas the global model uses a single function to correct the radiometric variations between images. Furthermore, both local and global color discrepancies are reduced in the combined model.

Two typical approaches for radiometric normalization of SAR images are invariant pixel-based and statistical feature-based methods. The core idea of identical pixel-based techniques is to determine the radiometric relationship among images for radiometric normalization via the invariable pixels. Cauty et al. [26] employed orthogonal regression to normalize time-invariant data and leveraged the linear scale consistency of multivariate alteration detection to produce immutable pixels. Considering the effect of scattering noise on the relative radiance normalization (RRN) processing, Wang et al. [27] employed a bi-direction linear regression model to remove bias in RRN parameter estimation and achieved robust radiance normalization using recursive weighted least squares. As previously stated, the efficacy of such approaches is highly dependent on the accuracy of the unchanging pixels retrieved. Therefore, some more effective ways for identifying immutable pixels have been presented. de Carvalho Jr et al. [28] used an optimal linear regression model that effectively suppresses outliers to achieve automatic acquisition of a large and sufficient number of pseudo-invariant characteristics. Ya'allah and Saradjian [29] utilized image difference histogram modeling via spectral bands to efficiently opt for unchangeable pixels.

Statistical feature-based strategies, on the other hand, make use of statistical data to calculate the radiometric mapping relationship between images in order to adjust for intensity consistency. By modifying the image's local mean and variance,

Hinse et al. [30] were able to create uniform intensity in various image regions. Shimada and Ohtaki [31] interpolated a gain correction factor that balances the intensities between adjacent bands using a polygonal curve approximation technique, and Shimada and Isoguchi [32] used histogram matching to modify the image gain to reduce the intensity differences between images. These techniques work well for processing images with similar content, as was previously indicated. The issue of error accumulation during radial propagation was recently resolved by Zhang et al. [6] using a random cross-observation technique. They were also able to achieve intensity correction for a range of high-resolution images using a regionally independent linear model, in accordance with a low-resolution reference image that was created. Furthermore, by employing a global quantization technique along with a radiometric adjustment model, Liu et al. [33] successfully removed the radiative disparities in SAR image stitching.

The majority of existing techniques might overlook the issue of image enhancement because they concentrate on eliminating noticeable intensity variations across images. That is, if the original image's visual quality is low, these techniques might not be able to produce visually acceptable outcomes. Some algorithms advocate for image enhancement as postprocessing or preparation for global color correction [19], [34]. While pretreatment cannot ensure image quality following global color adjustments, postprocessing has the potential to undermine global color uniformity. As a consequence, it is difficult for these algorithms to balance minimizing color inconsistencies with enhancing image quality. Li et al. [35] employed a global energy optimization framework to simultaneously enhance image contrast and color consistency in order to solve this issue. Since improving image contrast invariably makes the differences between images more noticeable. Consequentially, this strategy makes it difficult to set the proper weights to balance both of them. The Retinex theory-based approach [36], [37], [38] is one of the many enhancement algorithms that may effectively enhance an image's details. It is commonly used to deal with low brightness and blurry images. Motivated by this, in order to optimize image quality and color consistency, this research proposes a color correction and naturalness restoration method for multiple images with uneven luminance.

The sum of our contributions is as follows.

- 1) To create uniform intensity transitions between images and to remove both global and local intensity disparities, a combination model is proposed.
- 2) To eliminate local color differences, we propose a weighting scheme used in multiband blending and apply the results from multiband blending to enhance the efficacy of the block-based Wallis strategy. The experimental outcomes demonstrate that this approach successfully reduces noticeable image seams.
- 3) In order to preserve as much of the image's detailed information as possible, we solely optimize color consistency and image quality for the illumination component of the image according to Retinex theory. To improve the performance of each algorithm, these two procedures are also carried out independently.

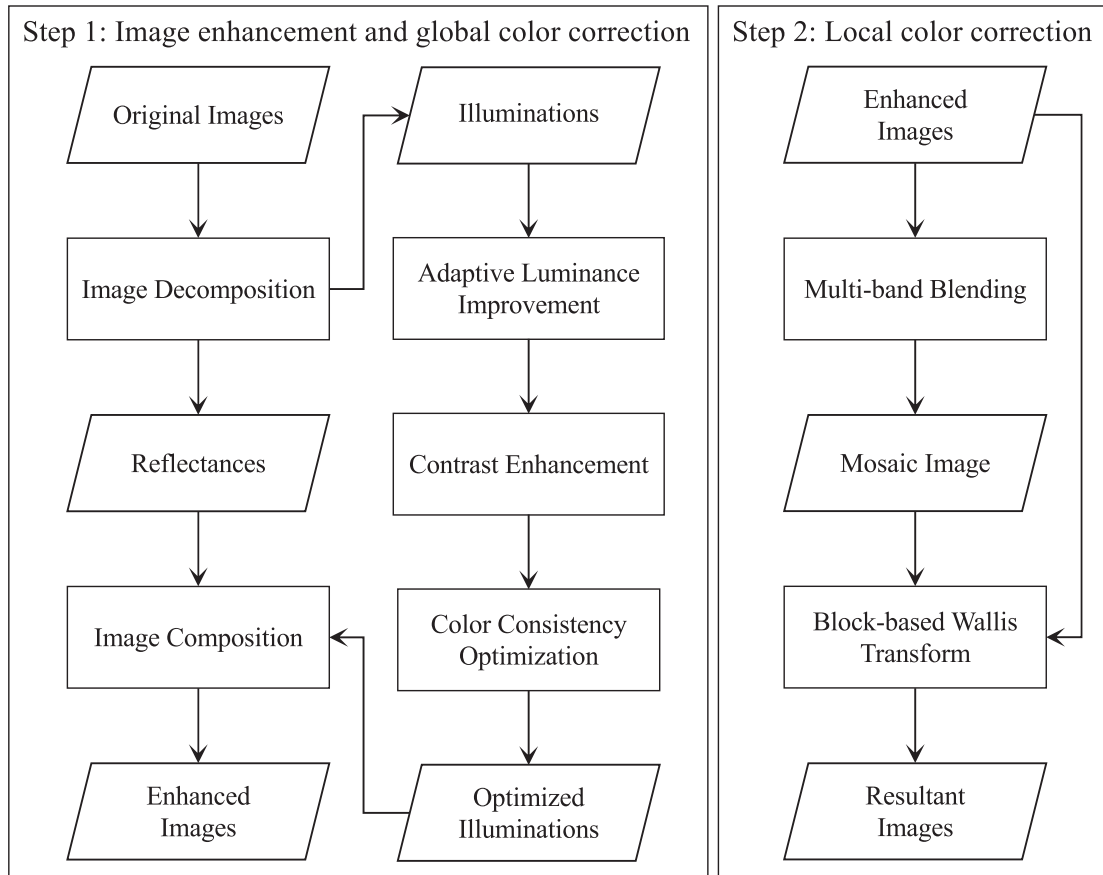


Fig. 1. Suggested approach's diagrams.

The rest of this article is structured as follows. Section II presents the suggested algorithms; Section III reports and discusses the experimental outcomes; and Section IV provides conclusions.

## II. PROPOSED METHOD

As shown in Fig. 1, the approach we propose is separated into two steps. The illumination components of the image are optimized in the first step, which includes enhancing the luminance distribution and contrast of the luminance components as well as decreasing the global intensity discrepancies between the luminance components. The enhanced image is then subjected to local color correction in the second step to smooth out any obvious seams between the images. The previously mentioned two steps are addressed in full below.

### A. Image Enhancement and Global Color Correction

Image quality is related to the human visual system. Finding a proper balance between naturalness and clarity makes it challenging to improve an image's clarity while maintaining its authenticity at the same time. The Retinex-based image enhancement methods that are now available can improve an image's clarity without sacrificing its natural appearance. As a result, at this stage, we also improve the image based on

Retinex theory and maximize image color uniformity. To be more specific, the image is first decomposed into two components: reflectance and illuminance. Among these, reflectance denotes local details, and illuminance denotes overall naturalness. Next, modules for adaptive brightness improvement, contrast enhancement, and color consistency optimization improve the image's illuminance. Finally, image composition is carried out, which multiplies optimized illuminance by reflectance to create an enhanced image. The details of the functional modules are provided below.

1) *Image Decomposition*: According to the Retinex theory, an image is made up of illuminance and reflectance. Many present techniques based on this notion use various filters, such as Gaussian filters or bilateral filters, to estimate the illuminance and consequently determine the reflectance. However, utilizing Gaussian filters directly to calculate illuminance causes issues with the results, such as halo artifacts around edges. To solve this, we blend the illuminance component retrieved by the Gaussian filter with the original image via the image gradient. Since the gradient precisely describes the difference between the image's intensity and illuminance component, it is possible to effectively control the halo effect by adjusting the extracted illuminance component.

The following are the precise steps: Initially, we acquire the low-frequency data  $L_I$  of image  $I$ , or the estimated illuminance

component, using Gaussian filtering. Subsequently, to decrease the effect of noise on the high-frequency data of image  $I$ , we employ the high-frequency data that has been processed by Gaussian filtering as the weighted map  $W$ , which can be determined using the subsequent formula

$$W(x, y) = (|I(x, y) - L_I(x, y)|) * G(x, y) \quad (1)$$

where  $G$  denotes the convolution kernel that was applied during the Gaussian filtering process, and  $I(x, y)$  and  $L_I(x, y)$  indicate the pixel values found at point  $(x, y)$  on image  $I$  and image  $L_I$ , respectively. We normalize the weighted map  $W$  after getting it to produce the weighted map  $W_N$ . The adjusted illumination component  $\tilde{L}_I$  is then determined using the following equation:

$$\tilde{L}_I(x, y) = W_N(x, y) \cdot I(x, y) + (1 - W_N(x, y)) \cdot L_I(x, y). \quad (2)$$

It is noteworthy that, in comparison to the single-scale Retinex method, the illuminance component  $\tilde{L}_I$  is more successful at safeguarding the edges and obfuscating the flat areas. Finally, by substituting  $\tilde{L}_I$  into the following equation, the reflectance  $R$  of the image can be obtained

$$R(x, y) = I(x, y) / \tilde{L}_I(x, y). \quad (3)$$

Furthermore, the majority of the image's detailed information is contained in the reflectance  $R$ .

2) *Adaptive Luminance Improvement*: To improve the image luminance, we employ a nonlinear function with a self-tuning parameter stated in the article by Sidike et al. [39] to avoid complicated computations. The following is the definition of this nonlinear function:

$$I_L(x, y) = \frac{\arctan(I_N(x, y)^\alpha - 0.5)}{2 \arctan(0.5)} + 0.5 \quad (4)$$

where  $I_N = I / I_{\max}$ ;  $I_N$  is the intensity image after normalization;  $I_{\max}$  represents the maximal value in image  $I$ ;  $I_L$  defines the grayscale image after luminance enhancement;  $I_L(x, y)$  indicates the value of the pixel positioned at  $(x, y)$ ; and  $\alpha$  represents the local adaptive parameter. Furthermore, the parameter computation utilizing the sigmoid function can provide reasonable enhancement of the image's dark and bright parts. The parameter can be calculated using the following formula:

$$\alpha(x, y) = \frac{1}{1 + e^{-I_N(x, y)}}. \quad (5)$$

According to the analysis of this nonlinear function, the shape of the function in the interval (0,1) resembles the shape of a power function with an exponent greater than 1. As a result, by maintaining the values of the bright regions while enhancing those of the dark parts, this module tends to recover richer information and improve the dark portions of the image. Finally, the results generated by this module need to be max-min-stretched to convert to 8-bit images.

3) *Contrast Enhancement*: An image's contrast will always drop when its brightness is increased. As such, to enhance the image's contrast, we use the idea of histogram equalization. But when the histogram contains obvious peaks and valleys, histogram equalization often leads to the issue of the image being over- or under-enhanced. To solve this problem, we employ

the methodology described in the research [35], creating the histogram with the support of gradient and contextual data. This method increases the percentage of edge pixels while decreasing the number of pixels in smooth areas by utilizing the gradient and neighborhood similarity of the pixels. Consequently, it successfully prevents artifacts caused by over- and under-enhancement from appearing. Please refer to the literature for specifics on the methodology. Next, using the created histogram as a basis, we calculate the probability density function  $p_o(\cdot)$  and define the uniform probability density function as follows:

$$p_u(l) = \frac{1}{256} \quad (6)$$

where  $l$  is the gray level and has a value range of [0,255]. The following equation is used for calculating the final probability density function  $p_r(\cdot)$ :

$$p_r(l) = w \cdot p_o(l) + (1 - w) \cdot p_u(l) \quad (7)$$

where  $w$  is the weighting coefficient. This coefficient is determined as follows and plays a crucial role in blending  $p_o(\cdot)$  and  $p_u(\cdot)$  in a sensible manner

$$w = \sum_{i=0}^{255} p_u(i) - p_{\text{clip}}(i) \quad (8)$$

where  $p_{\text{clip}}(\cdot)$  is derived by clipping the probability density function  $p_f(\cdot)$  in accordance with  $p_u(\cdot)$  as follows:

$$p_{\text{clip}}(l) = \begin{cases} p_u(l), & \text{if } p_f(l) > p_u(l) \\ p_f(l), & \text{otherwise} \end{cases} \quad (9)$$

where  $p_f(\cdot)$  is calculated via moving average filtering of  $p_o(\cdot)$  in the following manner:

$$p_f(l) = \frac{p_o(l) + p_o(l+1) + \dots + p_o(l+h-1)}{h} \quad (10)$$

where  $h$  indicates the size of the filtering window. Moving average filtering successfully smoothes out the spikes in the  $p_o(\cdot)$ . After getting the  $p_r(\cdot)$ , the following formula can be used for calculating the associated cumulative distribution function  $c_r(\cdot)$ :

$$c_r(l) = \sum_{i=0}^l p_r(i). \quad (11)$$

Finally, the enhanced image  $I_{\text{en}}$  is obtained by the transformation shown below

$$I_{\text{en}}(x, y) = \lfloor 255 \cdot c_r(I(x, y)) + 0.5 \rfloor. \quad (12)$$

The cumulative distribution function, in other words, is used as the grayscale remapping function.

4) *Color Consistency Optimization*: To decrease global color discrepancies among images, we translate the requirement to eliminate color discrepancies into parametric representations. The color remapping function  $f_i$  for each image is found by

solving the stated cost function using convex quadratic programming. The following is the designed cost function:

$$E = \sum_{\mathbf{I}_i \cap \mathbf{I}_j \neq \emptyset} E_{\text{color}}(\mathbf{I}_i, \mathbf{I}_j) + \lambda \sum_{i=1}^N E_{\text{regular}}(\mathbf{I}_i) \quad (13)$$

where  $\mathbf{I}_i$  and  $\mathbf{I}_j$  are the two overlapping input images. The coefficient of balancing the regularity and color terms is denoted by  $\lambda$ . For images  $\mathbf{I}_i$  and  $\mathbf{I}_j$ , the color term has been described as follows:

$$E_{\text{color}}(\mathbf{I}_i, \mathbf{I}_j) = \sum_{k=1}^K \left\| f_i(v_k^i) - f_j(v_k^j) \right\|_2 \quad (14)$$

where  $K$  represents the amount of color correspondences extracted, usually  $K = 16$ , and  $\|\cdot\|_2$  is the  $L_2$  norm.  $(v_k^i, v_k^j)$  denotes the  $k$ th color correspondence between  $\mathbf{I}_i$  and  $\mathbf{I}_j$ . The color correspondence is defined as the equal probability quantile corresponding to the two cumulative distribution functions computed in the overlap region of  $\mathbf{I}_i$  and  $\mathbf{I}_j$ . This is similar to obtaining a grayscale mapping between original and reference images in the histogram matching algorithm. The color term allows for the closest achievable grayscale distribution between the corrected images. It helps in the reduction of color discrepancies between images. As confining the remapping function alone with the color term leads to no solution and an invalid solution, we add the regular term to further constrain the remapping function, which is defined as follows:

$$E_{\text{regular}}(\mathbf{I}_i) = \sum_{i=1}^{M-1} \left\| f_i(\dot{v}_i^i) - \dot{v}_i^i \right\|_2 \quad (15)$$

where  $\dot{v}_i^i = (c_i^i + c_{i+1}^i)/2$ , and  $(c_i^i, c_{i+1}^i)$  denotes the anchor point coordinates that generate the segmented quadratic spline curve, the remapping function.  $M$  anchor points are typically used to generate the remapping function. The regular term's duty, in addition to ensuring the validity of the solution, is to allow the corrected image to have a color tone similar to the original image. Furthermore, a qualifying color remapping curve must meet two basic requirements: it must be monotonically growing, and the mapped values must be in the image's color domain. As a result, we apply the same limitations to the remapping curve as described in the article by Xie et al. [10] as follows:

$$C_{\text{rigid}}(f_i) : \begin{cases} \tau_l \leq f'_i(v_k^i) \leq \tau_u, \forall v_k^i \in [v_s, v_e] \\ v_{\min} \leq f_i(u_{0.01}^i), f_i(u_{0.99}^i) \leq v_{\max} \end{cases} \quad (16)$$

The cost function  $E$  is then solved using convex quadratic programming to derive the remapping function parameters for each image. Finally, color discrepancies across images are corrected using the remapping function.

### B. Local Color Correction

A global color consistency optimization method is utilized in Section II-A to lessen the variations in intensity across the SAR images within the study area. However, even after global color correction, there were considerable intensity discrepancies at the margins of neighboring images. We analyzed the reason for this occurrence and devised a focused response.

Due to the influence of the imaging technique, the edges of the SAR image in the range direction tend to display an inconsistent intensity distribution and thus need to have gain compensated. Furthermore, as SAR images are frequently affected by noise, the noise around the edge in the distance direction is enhanced during the antenna direction map correction procedure, giving this edge a larger radiation intensity than the central region. SAR images typically overlap each other within the study area. As a result, pixels toward the margins of an aberrant intensity image may appear in the middle of other normal-intensity images. In order to further smooth out the evident seams between images, we applied mutual intensity correction to the areas where adjacent images overlapped. To be more specific, we use multiband blending to first stitch together all of the images that need to be processed into a seamless mosaic. Subsequently, the local color disparities of the images are eliminated using a block-based *Wallis* transform, which makes the corrected images' intensity distribution resemble that of the mosaic images and removes any visible splicing traces between images. The aforementioned algorithm is explained in depth in the section that follows.

1) *Multiband Blending*: The fundamental idea of multiband blending is to create a mosaic image by superimposing the blended results after blending the overlapping areas of the image using various weights on different frequency bands. When blending various frequency bands, a different step size is needed for the weights' 0–1 transition, and this step size needs to match the frequency band's scale. In other words, the step size should be greater to prevent ghosting when dealing with lower scales of frequencies and smaller to minimize visual discontinuities when working with larger scales of frequency bands. The algorithm's steps are as follows.

Constructing the input images' Gaussian pyramid is the first step. Our approach sets the size of the Gaussian kernel used in each layer to  $5 \times 5$ , and it contains a single image in each of the five layers of the Gaussian pyramid. The Gaussian pyramids of images A and B, assuming that these are the input images, are represented as  $G_0^A, G_1^A, G_2^A, G_3^A, G_4^A$ , and  $G_0^B, G_1^B, G_2^B, G_3^B, G_4^B$ , respectively. In the second step, the input image's Laplace pyramid is computed. Below is the calculation formula

$$L_i = \begin{cases} G_i, & \text{if } i = 4 \\ G_i - F_u(G_{i+1}), & \text{otherwise} \end{cases}, \text{ for } i = 0, 1, 2, 3, 4 \quad (17)$$

where  $F_u(\cdot)$  denotes the up-sampling function,  $L_i$  and  $G_i$  denote the  $i$ th layer of the Laplace and Gaussian pyramids, respectively, and  $F_u(G_{i+1})$  has the same size as  $G_i$ . The Laplace pyramids of images A and B are labeled as  $L_0^A, L_1^A, L_2^A, L_3^A, L_4^A$ , and  $L_0^B, L_1^B, L_2^B, L_3^B, L_4^B$ , respectively. In the third stage, the overlapping regions of  $L_i^A$  and  $L_i^B$  are weighted-blended using a linear fusion technique.  $L_0^c, L_1^c, L_2^c, L_3^c$ , and  $L_4^c$  are the fused outcomes, accordingly. In the fourth phase,  $L_1^c, L_2^c, L_3^c$ , and  $L_4^c$  are sequentially up-sampled to the same size as  $L_0^c$ , and then  $L_0^c$  and all up-sampled results are superimposed to generate the final mosaic image.

A very critical step in the multiband blending algorithm is how to determine the weights of the pixels in the overlapping

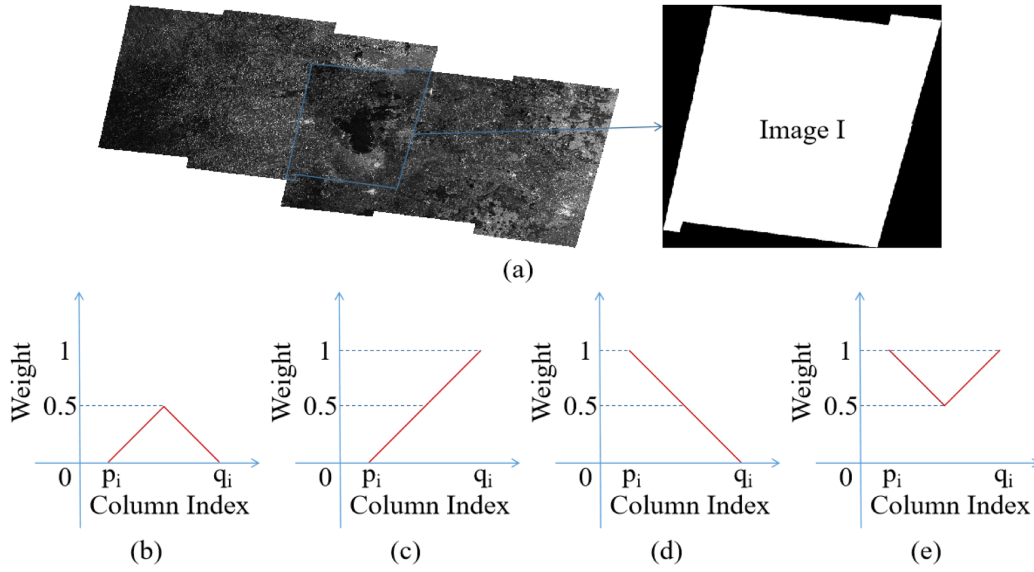


Fig. 2. (a) Overlapping region between the images. (b)–(e) Four cases showing the distribution of the pixel's weights.

region. For overlapping regions with regular shapes, it is easier to determine the weights. For example, you can simply specify that the weights of the pixels within the rectangular overlapping area are to be incremented or decremented in top-to-bottom or left-to-right order. However, the overlap region between orthophotos is usually irregular. Therefore, we propose a strategy for determining the weights of pixels in irregularly overlapping regions. The method has a total of three steps. Assume that image I of size  $M \times N$  is an overlapping region between images, as shown in Fig. 2(a).

*Step 1:* From row 0 to the  $M$ -1st row of pixels, each row of pixels gets processed in left-to-right order. The column indexes of the pixels having nonzero values are noted first as one traverses each row of pixels.  $N$  mutually disjoint sets can be formed by these column indexes. For instance,  $\mathbb{Q}_i = \{x_i \mid x_i \in [p_i, q_i], p_i < q_i, x_i, p_i, q_i \in [0, N - 1] \cap \mathbb{N}\}$ ,  $i \in \{1, 2, \dots, n\}$ , where  $p_j > q_{j-1} + 1, j \in \{2, 3, \dots, n\}$ . In addition, assuming the current row number is  $r$ , condition one is  $p_i = 0$ , or  $I(r, p_i - 1) = 0$ , and condition two is  $q_i = N$ , or  $I(r, q_i + 1) = 0$ . Then, determine the weight of the pixel whose column index is a part of set  $\mathbb{Q}_i$  by applying the next four rules.

- 1) If both condition one and condition two hold, then the distribution of pixel weights appears as illustrated in Fig. 2(b).
- 2) If condition one holds and condition two does not, then the distribution of pixel weights looks as displayed in Fig. 2(c).
- 3) If condition two holds and condition one does not, then the distribution of pixel weights is presented in Fig. 2(d).
- 4) If neither condition one nor condition two holds, then the distribution of pixel weights is shown in Fig. 2(e).

*Step 2:* Starting from column 0, traverse each column of pixels in top-to-bottom and left-to-right order until the  $N$ -1th column of pixels has been processed. As one traverses each column of

pixels, the method in step one is used to determine the weights of each pixel.

*Step 3:* The average of the pixel weights determined in the above two steps is taken as the final weights of the pixels.

2) *Block-Based Wallis Transform:* The principle behind the Wallis transform is to employ the reference image to modify the average and standard deviation of the original image, bringing the original image's hue consistent with that of the reference image. The general description of this transformation is as follows:

$$I_{\text{out}}(r, c) = [I_{\text{in}}(r, c) - m_{\text{in}}] \frac{s_r}{s_{\text{in}}} + m_r \quad (18)$$

where  $I_{\text{in}}(r, c)$  and  $I_{\text{out}}(r, c)$  are pixel values at point  $(r, c)$  in the input and output images, respectively. The means of the input and reference images are denoted by  $m_{\text{in}}$  and  $m_r$ , respectively, and the standard deviations are represented by  $s_{\text{in}}$  and  $s_r$ . The preceding equation explains how the Wallis transform achieves global color correction by utilizing statistical characteristics (e.g., mean and standard deviation). To achieve local color correction, we first block the image and then apply the Wallis transform to each image block. When it comes to image blocking, both the reference and original images should be blocked using the same strategy. In order to eliminate the block effect in the output images, bilinear interpolation is used to compute each pixel's standard deviation and average for the original and reference images.

The following are the precise steps: First, figure out each image block's statistics. Subsequently, the statistical information of the four corner points of the image block gets determined as the average of the statistics of the image block to which they belong. It is worth noting that statistics with zero values should be disregarded when calculating corner-point statistics.

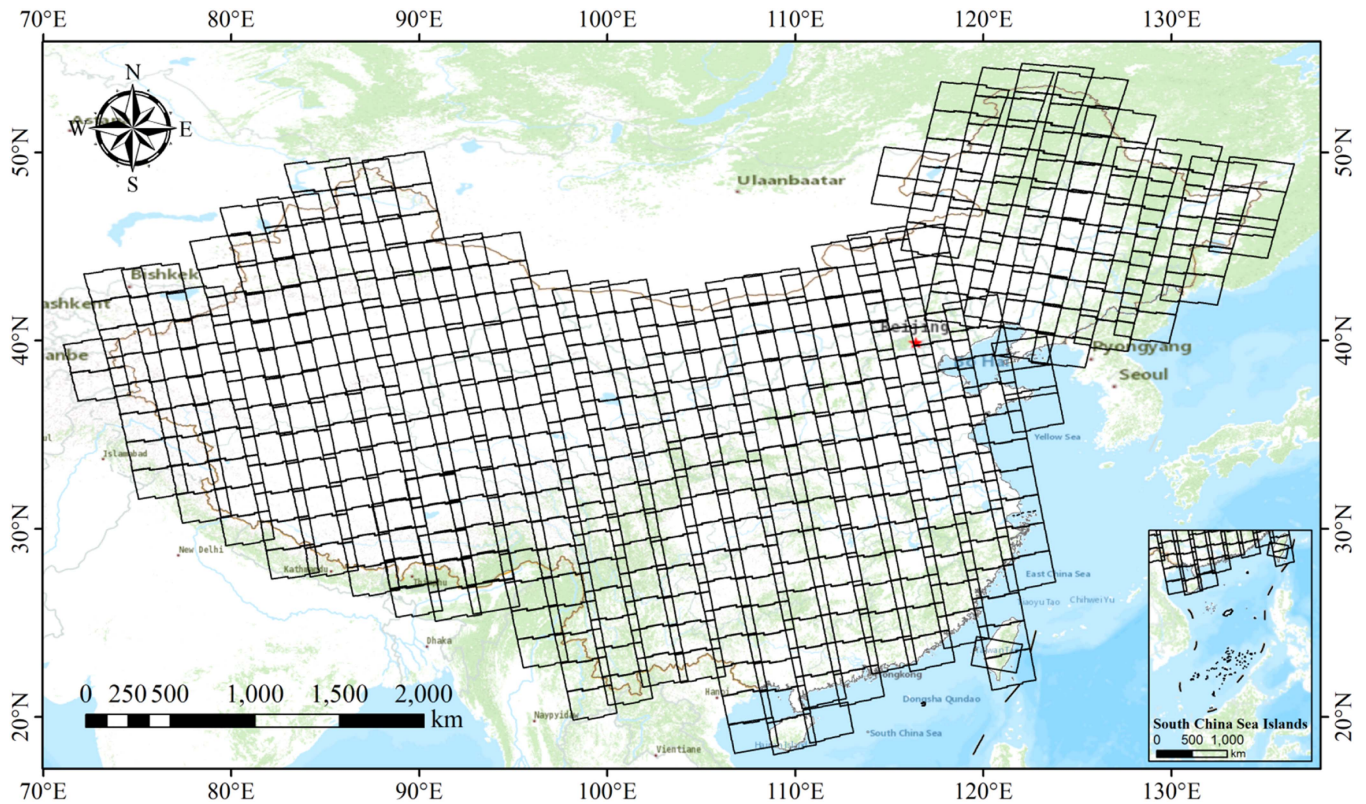


Fig. 3. Sentinel-1 SAR images covering most of China's land area.

Finally, bilinear interpolation is utilized to determine the statistical characteristics of each pixel based on the data from the image block's four corner points. Next, in order to achieve a smooth intensity transition and remove the obvious splicing seams between the images, the *Wallis* transform is carried out on the original image's pixels in accordance with (18). Notably, in order to maintain the original image's textural features, we process the image's low-frequency data using the block-based *Wallis* method rather than the image itself. Stated differently, we used a Gaussian filter to first split the image into its low- and high-frequency data. Next, we use the low-frequency information from the reference image to alter that of the original image using a block-based *Wallis* transform. The final image is then created by combining the source image's high-frequency data with the processed result.

### III. EXPERIMENTS

#### A. Experimental Datasets

402 Sentinel-1 single-polarized SAR images in interferometric wide swath mode and 9 Gaofen-3 (GF-3) unipolarized SAR images in fine-strip 2 mode were chosen as datasets for the study. Fig. 3 illustrates the coverage of Sentinel-1 SAR images. Table I displays the specifics of these datasets. It takes up roughly 158 GB of RAM to store these images. The coordinate system of the images is unified as WGS-84. These datasets contain images from different seasons and shooting methods. Due to seasonal differences, the backscatter coefficients between

TABLE I  
BASIC INFORMATION ON THE DATASETS

| Dataset Name          | CHINA                     | TAIHU                     |
|-----------------------|---------------------------|---------------------------|
| Image Num.            | 402                       | 9                         |
| Image Mean Width      | 25704                     | 15187                     |
| Image Mean Height     | 16219                     | 14158                     |
| Imaging Time Span     | 2019.10.04–<br>2021.08.12 | 2018.04.21–<br>2019.01.02 |
| Incidence Angle Range | 38.70~39.67 °             | 19 ~50 °                  |
| Image Resolution      | 15 m                      | 10 m                      |
| Platform              | Sentinel-1                | Gaofen-3                  |

images exhibit significant inconsistencies. In addition, different shooting methods, such as shooting when the orbit rises or falls, can also cause significant radiation differences between images. Therefore, through these challenging datasets, we can effectively test the performance of different algorithms.

#### B. Evaluation Metrics

In this study, the effectiveness of color-correcting algorithms is statistically evaluated using three objective indicators. The color distance (CD), which is used to assess how well various methods remove color discrepancies across images, is the first

evaluation metric. The difference in color between images reduces with decreasing CD values. The average gradient (AG) of the image serves as the second metric. This metric is used to measure how well an image reflects the sharpness of small features. Generally speaking, a larger AG denotes a sharper, higher-contrast image. The third metric is the patch-based contrast quality index (PCQI). This indicator compares the contrast change and structural similarity of two images. That is, the amount of contrast enhancement and structural distortion in the resulting image when compared to the original image. A higher PCQI value indicates a stronger contrast in the resulting image.

1) *Color Distance*: For two overlapping color-corrected images,  $\mathbf{I}_p$  and  $\mathbf{I}_q$ , this indicator is defined as follows:

$$\text{CD}(\mathbf{I}_p, \mathbf{I}_q) = \sqrt{\frac{\sum_{k=1}^K (v_k^p - v_k^q)^2}{K}} \quad (19)$$

where  $(v_k^p, v_k^q)$  represents the  $k$ th color correspondence between  $\mathbf{I}_p$  and  $\mathbf{I}_q$ .  $K$  denotes the number of color correspondences, which is usually 16.  $v_k^p$  and  $v_k^q$  denote the quantile with probability  $k/(K+1)$  of the cumulative distribution function in the overlapping regions  $\mathbf{I}_{pq}$  and  $\mathbf{I}_{qp}$ , respectively.  $\mathbf{I}_{pq}$  denotes the area of  $\mathbf{I}_p$  overlapped with  $\mathbf{I}_q$ .  $\mathbf{I}_{qp}$  also has a similar meaning.

2) *Average Gradient*: The following is the calculation formula:

$$\text{AG}(\mathbf{I}) = \frac{1}{H \times W} \sum_{h=0}^{H-1} \sum_{w=0}^{W-1} \times \sqrt{\frac{(\mathbf{I}_{h,w} - \mathbf{I}_{h,w+1})^2 + (\mathbf{I}_{h,w} - \mathbf{I}_{h+1,w})^2}{2}} \quad (20)$$

where  $W$  and  $H$  denote the image's width and height, respectively.  $\mathbf{I}_{h,w}$  represents the pixel's value at the image's position  $(h, w)$ .

3) *Patch-Based Contrast Quality Index*: This indicator can be described as follows:

$$\text{PCQI}(\mathbf{X}, \mathbf{Y}) = \frac{1}{N} \sum_{i=1}^N q_c(\mathbf{X}_i, \mathbf{Y}_i) \cdot q_s(\mathbf{X}_i, \mathbf{Y}_i) \quad (21)$$

where both images  $\mathbf{X}$  and  $\mathbf{Y}$  are divided into  $N$  nonoverlapping patches.  $\mathbf{x}_i$  and  $\mathbf{y}_i$  are patches located at the same position in image  $\mathbf{X}$  and image  $\mathbf{Y}$ , respectively.  $q_c(\mathbf{x}, \mathbf{y})$  is used for assessing the degree of contrast enhancement of patch  $\mathbf{y}$  over patch  $\mathbf{x}$ .  $q_s(\mathbf{x}, \mathbf{y})$  is used to compare the structural similarity of patches. For detailed definitions of  $q_c(\mathbf{x}, \mathbf{y})$  and  $q_s(\mathbf{x}, \mathbf{y})$ , please refer to the article by Wang et al. [40].

### C. Experimental Results Analysis

1) *Global Comparison*: This part presents a comparison between the outcomes obtained from the proposed strategy and the other two methods. The first approach is called color correction with gradient preservation (CCGP) [10], which enhances image quality using terms for dynamic range and gradient. The dynamic range term in this method improves image contrast by extending the range of color assignments, while the gradient term keeps the image features. Another method is Contrast-Aware

Color Consistency Correction (CACCC) [35], which effectively addresses the issues of the image's over- and under-enhancement and increases the image contrast with the designed contrast term. CCGP is less beneficial for single-band images, so we made changes to the source code from the article by Xia et al. [10] while retaining the original parameter settings. In addition, CACCC needs to determine two parameters,  $\lambda_1$  and  $\lambda_2$ , and different parameter values will result in various outcomes. When  $\lambda_1 = 0.1$  and  $\lambda_2 = 0.9$ , the result is most visually appealing and is chosen as the experimental data. The two strategies mentioned above are highly valuable in comparison for lowering color inconsistency between images and enhancing image quality.

As the computational cost of directly processing high-resolution SAR images is very high, we down-sampled the original images by a factor of 10 using the average-based down-sampling technique, which can be adjusted to meet practical requirements. An image with  $29\,360 \times 16\,234$  pixels, for example, is down-sampled to  $2936 \times 1624$  pixels. The downsampled images are then processed. In addition, for comparison with high-resolution images generated by other methods, we have utilized the approach proposed in our prior work [41] to decrease the color disparities between the high-resolution raw images, where the strategy uses a low-resolution reference image created by the methodology suggested in this article. It is noteworthy that we did not use the first step of the approach to optimize the reference image; instead, we processed the source image directly using the second step. For further details, please see that article. Next, we analyzed the experimental data both numerically and visually.

Fig. 4(a) illustrates the research area's source images. The intensity of the images positioned at different locations varies noticeably. The CCGP outcomes are depicted in Fig. 4(b), and we notice that intensity variations between images are well suppressed; however, there are still visible stitching seams between images, indicating that CCGP focuses mostly on global intensity disparities and does not precisely correct local intensity discrepancies for images within the study region. The CACCC results are shown in Fig. 4(c), with a better visualization of the intensity distribution throughout the research area. The method effectively improves the image's sharpness. However, like CCGP, the approach mainly concentrates on global color differences and does not properly smooth intensity discrepancies at the image's boundaries. The results processed by our approach are shown in Fig. 4(d), where the whole study region is better visualized, with natural and seamless intensity transitions between images, greatly improved image quality, and enhanced overall image hierarchy.

Table II displays the results of the quantitative assessment of the various approaches to the experimental data. According to the statistical results, images processed by our method outperform CCGP and CACCC in all three criteria, which is consistent with the visual performance. Only in metric CD is the CACCC inferior to the CCGP. This is because the approach must make a compromise with regard to image contrast enhancement and color consistency optimization, i.e., sacrificing metric CD accuracy to improve image quality. Since CCGP tends to lower visual contrast to maintain the image's tonal consistency, the



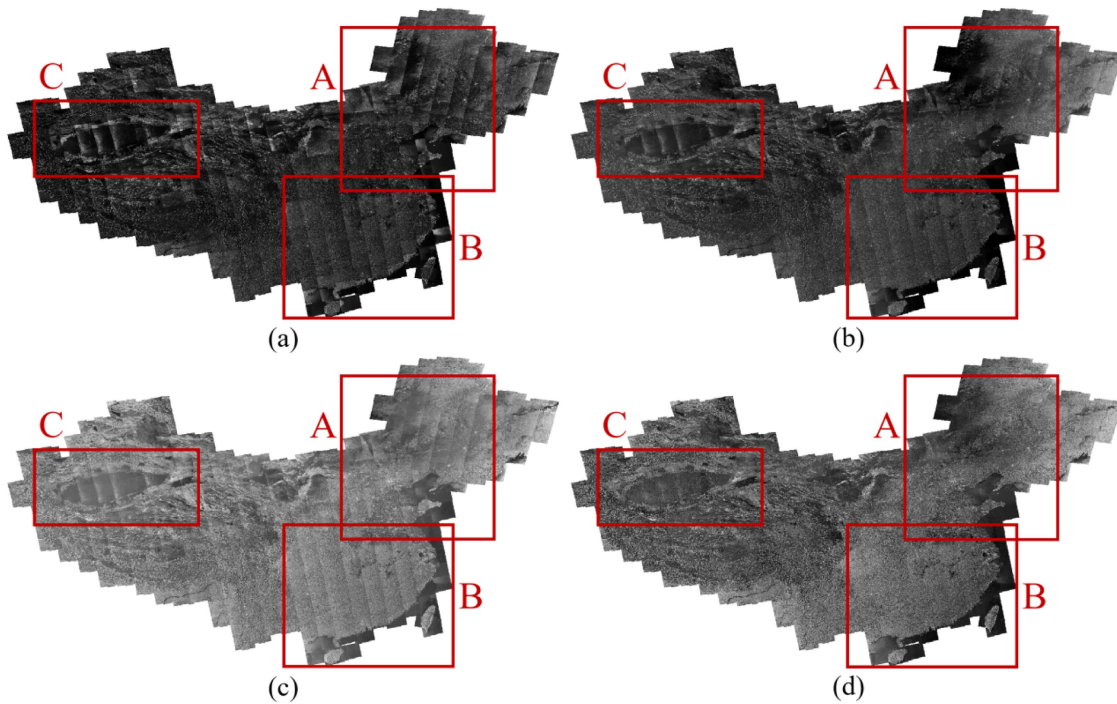


Fig. 4. Experiment outcomes based on the China dataset. (a) Initial images. (b) and (c) Outcomes generated via the CCGP and CACCC approaches, respectively. (d) Outcome corrected through our method. To effectively assess methodologies, outcomes from the dataset in the A, B, and C areas were selected for further analysis.

TABLE II  
QUANTITATIVE RESULTS OF VARIOUS METHODS ON THE CHINA DATASET

| Methods | CHINA Dataset |          |         |
|---------|---------------|----------|---------|
|         | CD            | AG       | PCQI    |
| Input   | 30.94818      | 14.99889 | --      |
| CCGP    | 14.27874      | 13.48412 | 0.88667 |
| CACCC   | 16.71301      | 16.63027 | 0.89936 |
| Ours    | 9.74477       | 28.21346 | 1.18627 |

approach generates images that are superior to the original image in terms of metric CD but inferior in terms of metric AG.

To further investigate and assess the various approaches, we chose images from the China dataset located in areas A, B, and C of Fig. 4, which present significant radiance variations caused by orbital differences, antenna azimuth map variations, and imaging processor gain errors. The three trial sets enable us to precisely analyze the efficacy of several strategies on images from different geographies. Table III shows the quantitative analysis outcomes of the different strategies for the three regions.

Fig. 5 displays the results of the color correction for region A. The original images located in various tracks exhibit noticeable intensity discontinuities prior to algorithmic processing, as can be seen. While the global color discrepancies have been eliminated in Fig. 5(b) and (c), there are still noticeable intensity differences between images in the red box and issues with too dark and low contrast images in the blue box, respectively. Fig. 5(c)

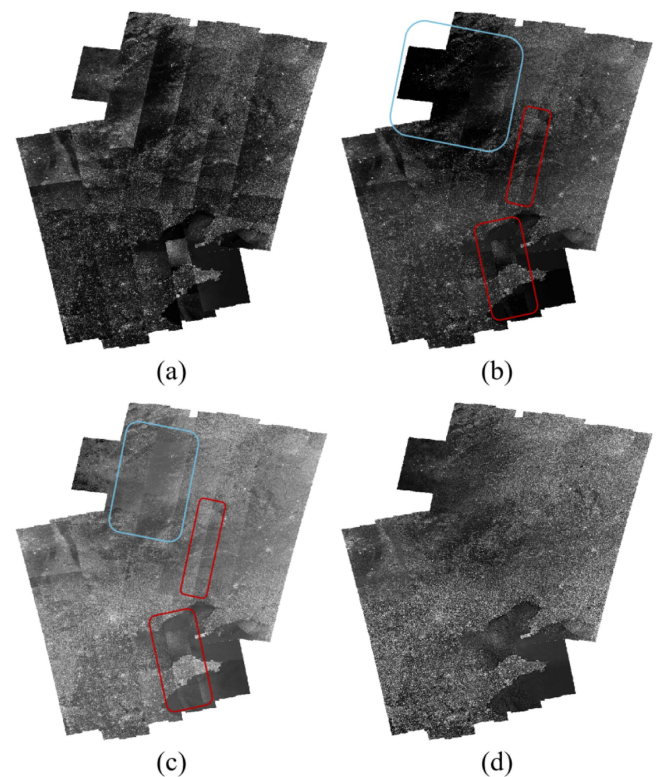


Fig. 5. Analysis of outcomes achieved through images from Region A. (a) Initial images. (b) and (c) Outcomes corrected through the CCGP and CACCC approaches, respectively. (d) Outcome produced via our method. The blue box represents areas with low contrast and severe darkness, whereas the red boxes indicate notable color differences.

TABLE III  
QUANTITATIVE OUTCOMES OF MULTIPLE METHODS ON RESEARCH DATA IN THE A, B, AND C REGIONS

| Methods | Region A |          |         | Region B |          |         | Region C |          |         |
|---------|----------|----------|---------|----------|----------|---------|----------|----------|---------|
|         | CD       | AG       | PCQI    | CD       | AG       | PCQI    | CD       | AG       | PCQI    |
| Input   | 40.07423 | 15.90965 | --      | 32.17899 | 17.08734 | --      | 41.64908 | 12.66705 | --      |
| CCGP    | 16.85903 | 13.86346 | 0.83905 | 15.03782 | 15.89852 | 0.86308 | 18.16314 | 10.41890 | 0.85390 |
| CACCC   | 17.21885 | 13.70176 | 0.79938 | 17.43299 | 18.22245 | 0.91276 | 18.59025 | 12.22551 | 0.84846 |
| Ours    | 8.28369  | 23.66052 | 1.13140 | 8.30819  | 30.37593 | 1.19054 | 12.17319 | 28.55418 | 1.29201 |

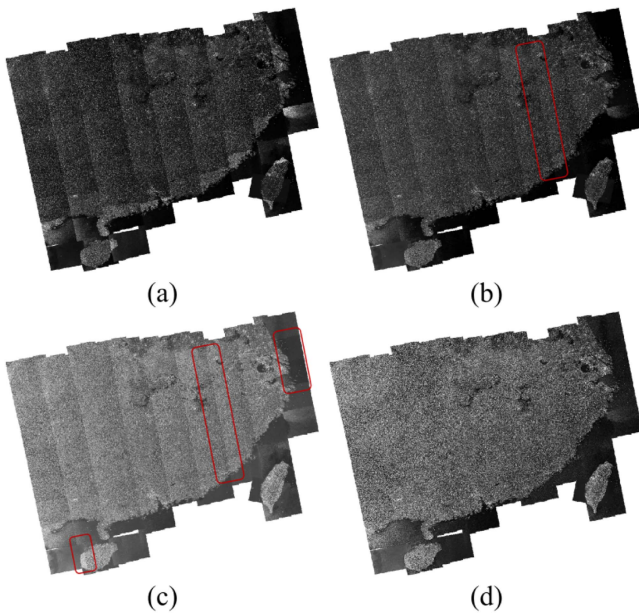


Fig. 6. Experimentation results acquired with images in Region B. (a) Initial images. (b) and (c) Outcomes corrected through the CCGP and CACCC methods, respectively. (d) Outcome corrected via our method. The red boxes present noticeable color discrepancies.

has a better general distribution of brightness but is slightly less sharp than Fig. 5(b). As seen within Fig. 5(d), the proposed approach improves the intensity consistency of this region when compared to previous algorithms, leaves no evidence of intensity differences, and produces an image with greater sharpness and texture details. The quantitative outcomes in Table III indicate that our strategy outperforms all other methods in all metrics. This is in accordance with the qualitative assessments shown above and demonstrates the efficacy of the suggested approach. The CACCC has a disadvantage in all indicators when compared to the CCGP. It indicates that when processing images covering a vast area, the approach is less stable in improving image contrast. As previously stated, the method's lowering of image contrast causes the large gap between the results obtained by CCGP and the original images in the metric AG.

The initial and processed images for region B are displayed in Fig. 6. It is straightforward to see that Fig. 6(d) is preferable to

Fig. 6(b) and (c), both in terms of image quality and uniformity of intensity. The issue with the noticeable color transition in the region of the red box within Fig. 6(b) remains. Although the overall brightness distribution and image clarity in Fig. 6(c) are significantly improved over Fig. 6(b), the intensity inconsistency across the images is also increased, as seen by the red box. In terms of quantitative evaluation, Fig. 6(d) demonstrates considerable advantages across all criteria. In comparison to Fig. 6(b), Fig. 6(c) cannot account for all metrics and only performs better on the metrics AG and PCQI. This illustrates the algorithm's weaknesses.

Fig. 7 exhibits the color-correcting results of various approaches on images from region C. Overall, all methods minimize image intensity discrepancies to varied degrees. Since the CCGP and CACCC only reduce global intensity differences across images, Fig. 7(b) and (c) still show significant local color disparities in some locations, such as those denoted by red boxes. Furthermore, while Fig. 7(c) has greater general sharpness than Fig. 7(b), there is an issue with low contrast within the blue box region. As shown in Fig. 7(d), our strategy produced the most pleasing visual results. The statistical results in Table III offer support for this statement.

In conclusion, CCGP fails to produce good-quality images when the visual quality of the original image is low, despite being supposed to preserve image details and enhance image contrast through a gradient term and a dynamic range term, respectively. Similar to this, CACCC utilizes color and contrast terms to improve contrast and decrease intensity discrepancies between images. However, it is challenging for the method to simultaneously improve the consistency of intensity between images and visual contrast. As a result, neither approach can successfully improve the visual quality of images and poses certain limits. By enhancing contrast and brightness and conducting global color correction on only the luminance component of the image, the proposed approach improves image visual quality while efficiently maintaining image texture features. Furthermore, our method enforces local color correction to further smooth out the intensity discrepancies at the image's boundaries, resulting in visually acceptable correction outcomes.

In addition, we evaluate the proposed method on GF-3 images to demonstrate that the strategy is equally applicable to data acquired by other types of sensors. The qualitative and quantitative

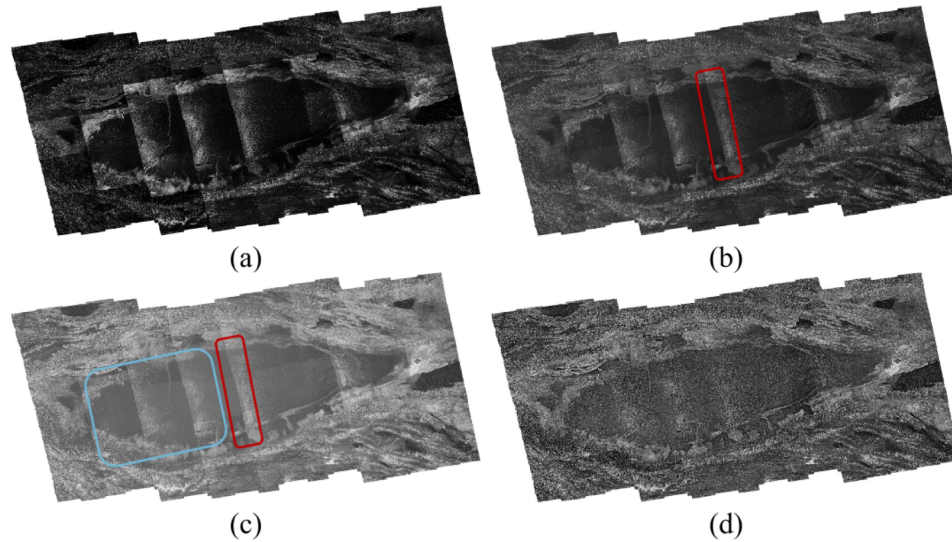


Fig. 7. Analysis of the outcomes obtained via images from Region C. (a) Initial images. (b) and (c) Outcomes generated with the CCGP and CACCC methods, respectively. (d) Outcome corrected through our method. The red box denotes regions with considerable differences in colors, and the blue box shows regions with low contrast.

TABLE IV  
QUANTITATIVE OUTCOMES OF VARIOUS METHODS ON THE TAIHU DATASET

| Methods | TAIHU Dataset |          |         |
|---------|---------------|----------|---------|
|         | CD            | AG       | PCQI    |
| Input   | 12.23324      | 20.49056 | --      |
| CCGP    | 4.82132       | 20.26346 | 0.99191 |
| CACCC   | 6.88457       | 42.45180 | 1.21761 |
| Ours    | 2.72390       | 29.03049 | 1.12996 |

results are shown in Fig. 8 and Table IV, respectively. Since the data processed by the proposed approach is grayscale images, the algorithm can theoretically process images acquired by different sensors without discrimination as long as the backscattering coefficients in the SAR images are linearly stretched to grayscale values.

As shown in Fig. 8(d), outperforms (b) and (c) in terms of grayscale consistency, particularly in the region indicated by the red boxes. Furthermore, the comparison of (c) and (d) demonstrates that, when compared to the CACCC, our method moderately enhances the image and effectively avoids amplifying noise in images. The quantitative results in Table IV support the above argument. Table IV shows that CACCC necessitates a trade-off between the metrics PCQI and CD when compared to CCGP, whereas our strategy optimizes both.

In conclusion, the above-mentioned experimental results are sufficient to show that our method is able to effectively process GF-3 data. The method provides favorable technical support for the production of visually pleasing mosaics based on SAR images from multiple sources.

2) *Detailed Analysis*: This section compares the suggested approach to the CACCC method and assesses its impact on the image's local features. Several sets of typical scene images, such

as those of plains, cities, mountains, and waters, make up the experimental data. Fig. 9 and Table V, respectively, exhibit the qualitative and quantitative results. As shown in Fig. 9, while processing images containing water, our approach is able to keep the precise information about the waters more efficiently than the CACCC method. This is so because our technique improves the illumination component of the image rather than the image itself. Furthermore, as noise frequently takes the form of high-frequency information in images, boosting the image's illuminance alone can effectively prevent noise from being amplified. As can be seen from the comparison of (b3) and (c3) in Fig. 9, our methodologies can effectively avoid magnifying the noise in the image when boosting the plains-containing image, in contrast to the CACCC approach.

The large CD values between the original image pairs, as shown in Table V, suggest that there are significant intensity differences between the source image pairings. Following processing by our approach and the CACCC methodologies, the value of CD decreased, but our technique performed better. This is because the image-overlapping areas contain different types of features that may have various radiometric correspondences with each other. Consequently, a single-spline curve model may be unable to take into consideration color discrepancies in local regions of the image. In addition, our method and the CACCC approach yield similar results for the metric PCQI. In this study, a global-to-local strategy is used to maximize the image's color consistency, and according to the Retinex theory, we only improve the brightness and contrast of the image's illuminance component. Thus, our approach produces better outcomes in terms of color constancy and image quality.

3) *Ablation Study*: In this section, we conduct ablation experiments on the images in region C to investigate the impacts of the proposed approach's image enhancement (IE), global color correction (GCC), and local color correction (LCC) on the experimental results. Methods 1–3 can be obtained by taking out

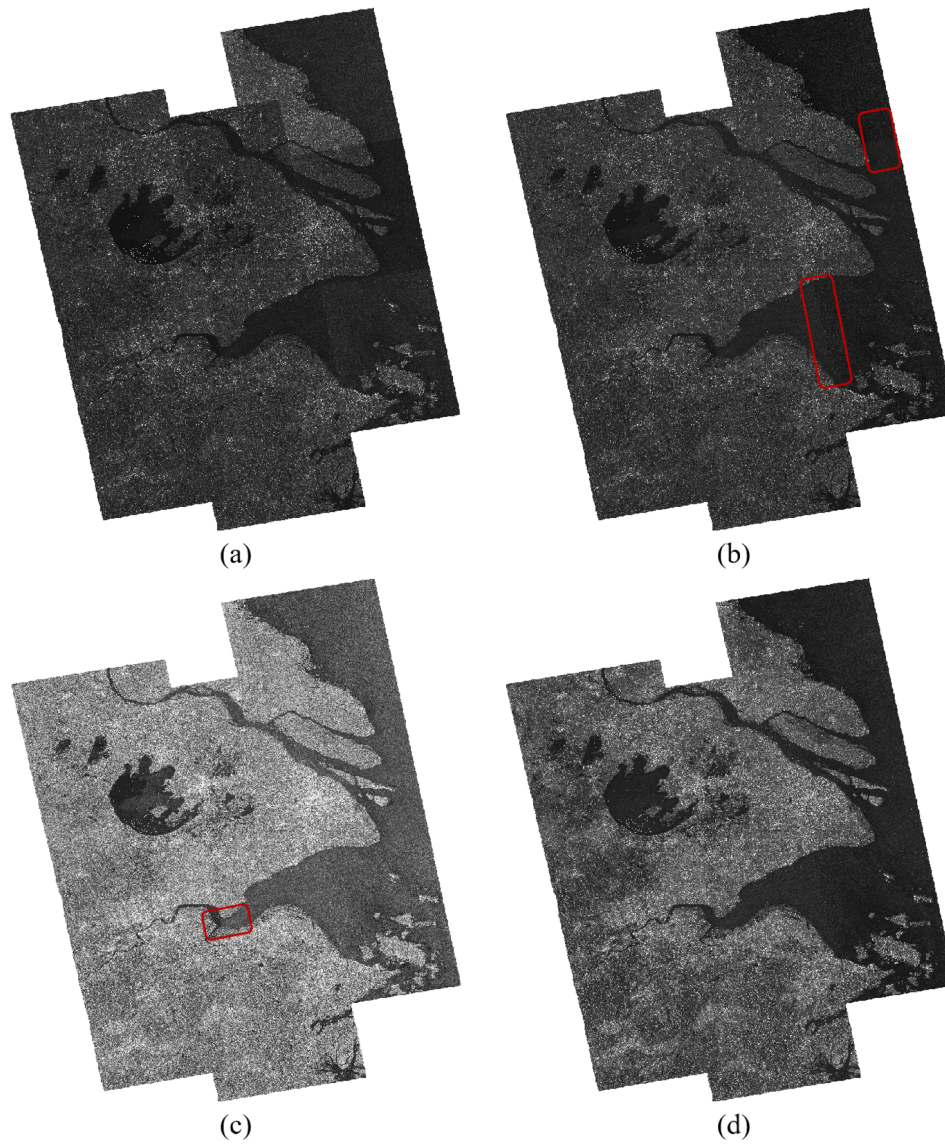


Fig. 8. Experiment outcomes based on the TAIHU dataset. (a) Original images. (b) and (c) Outcomes generated via the CCGP and CACCC methods, respectively. (d) Outcome obtained through our approach. The red boxes indicate clear color discrepancies.

TABLE V  
QUANTITATIVE RESULTS OF VARIOUS METHODS ON LOCALIZED INTENSITY BY SCENE AND IMAGE

| Scenes   | Images | Input    |      | CACCC    |         | Ours     |         |
|----------|--------|----------|------|----------|---------|----------|---------|
|          |        | CD       | PCQI | CD       | PCQI    | CD       | PCQI    |
| Mountain | I1     | 42.95307 | --   | 20.01855 | 1.10501 | 8.55682  | 1.07620 |
|          | I2     |          |      |          |         |          |         |
| Water    | I1     | 10.10581 | --   | 5.35086  | 0.92807 | 3.18248  | 0.98237 |
|          | I2     |          |      |          |         |          |         |
| City     | I3     | 19.11677 | --   | 13.20892 | 0.98441 | 12.17061 | 0.92188 |
|          | I4     |          |      |          |         |          |         |
| Plain    | I3     | 17.74341 | --   | 16.03112 | 1.11077 | 15.44126 | 1.05065 |
|          | I4     |          |      |          |         |          |         |

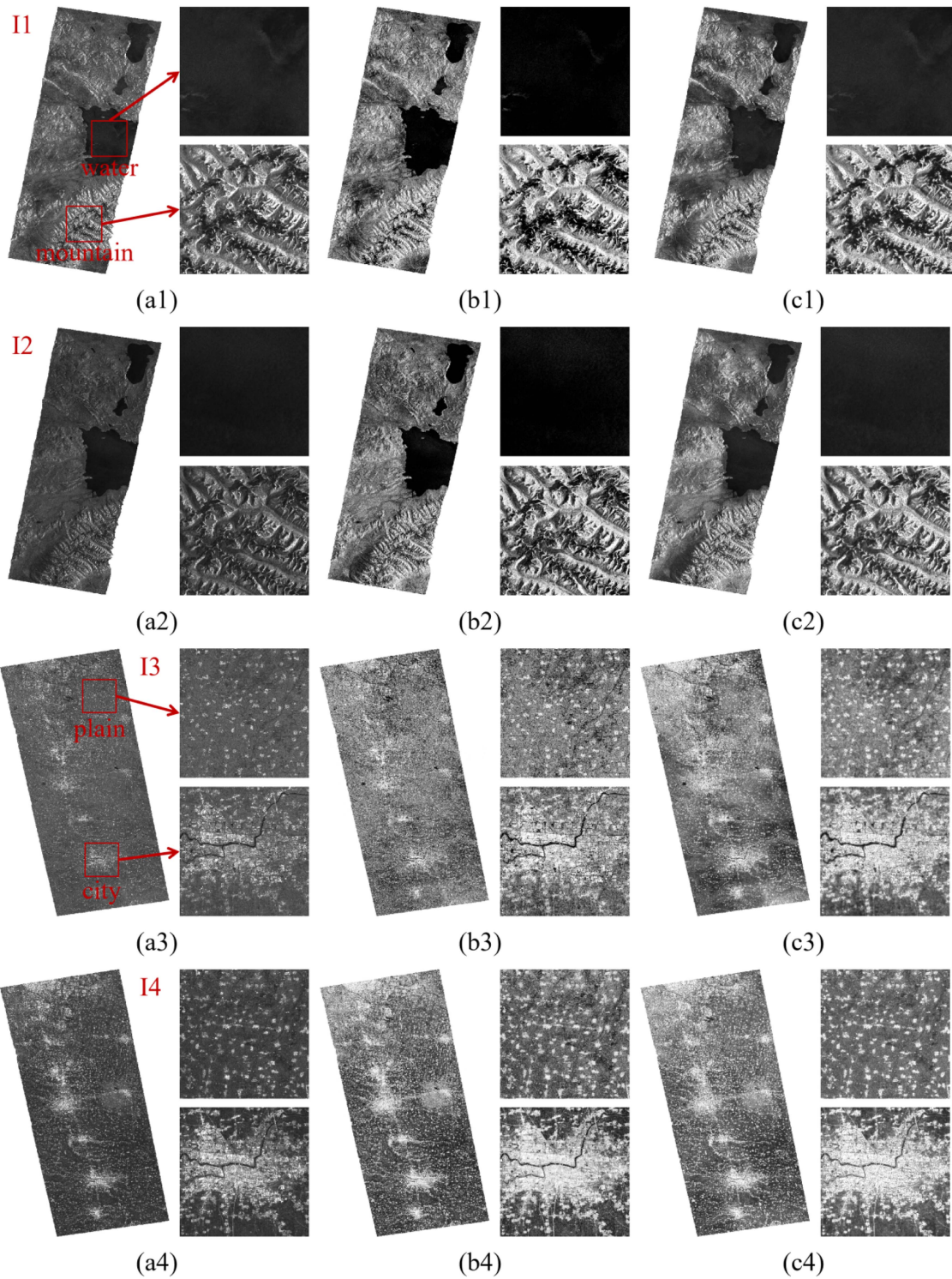


Fig. 9. Neighboring image overlapping regions and local magnifications. (a1) and (a2) Image pair 1 and detail views following CACCC method processing. (b1) and (b2) Image pair 1 and detail views following CACCC method processing. (c1) and (c2) Image pair 1 and detail views after processing by our approach. (a3) and (a4) Image pair 2 and local enlarged views. (b3) and (b4) Image pair 2 and detail views following CACCC approach processing. (c3) and (c4) Image pair 2 and detail views after processing by our method.

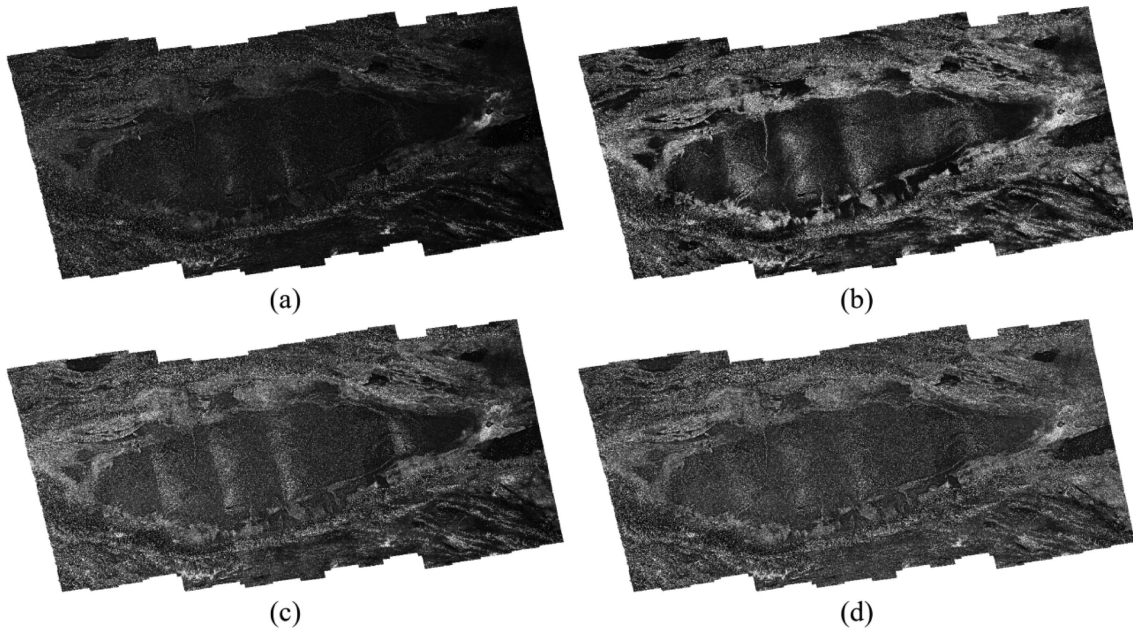


Fig. 10. Qualitative outcomes of ablation studies on images in region C. (a)–(c) Outcomes generated with methods 1–3, respectively. (d) Outcome obtained through our method.

TABLE VI  
QUANTITATIVE RESULTS OF ABLATION EXPERIMENTS PERFORMED ON IMAGES  
LOCATED IN REGION C

| Methodologies      | Region C |         |
|--------------------|----------|---------|
|                    | CD       | PCQI    |
| Method 1 (GCC+LCC) | 6.46696  | 1.06396 |
| Method 2 (IE+LCC)  | 24.38654 | 1.26388 |
| Method 3 (IE+GCC)  | 20.01257 | 1.26671 |
| Ours (IE+GCC+LCC)  | 12.17319 | 1.29201 |

IE, GCC, and LCC from the proposed approach, respectively. Table VI and Fig. 10 present the quantitative and qualitative findings, respectively.

Compared to Fig. 10(a), Fig. 10(d) has higher visual quality, indicating that IE can effectively enhance image quality. Nevertheless, according to the quantitative findings, IE improves the images while magnifying the color inconsistencies between them. Through a comparison of (b) and (d) in Fig. 10, we can observe that the use of GCC eliminates color discrepancies across images while reducing image contrast. Fig. 10(d) exhibits better intensity uniformity than Fig. 10(c), demonstrating that LCC can achieve uniform intensity transitions by removing local color disparities between images. However, LCC still suffers from reduced image contrast. Through a quantitative comparison between methods 1 and 2, as well as approaches 1 and 3, it is evident that the color correction algorithms (LCC, GCC)

outperform IE in terms of improving the metric CD but fall short of IE in terms of increasing the metric PCQI. It indicates that the goal of the color correction and image enhancement methods, respectively, is to improve color consistency and image quality. The quantitative outcomes of methods 2 and 3 can likely be compared, and it can be seen that while both have similar impacts on the improvement of the metric PCQI, LCC is not as effective as GCC in increasing the metric CD.

Overall, color inconsistencies across images can be effectively eliminated by both GCC and LCC, although GCC works better. Furthermore, the consistency of hue and image quality cannot be simultaneously optimized by IE or the color-correcting algorithm. We combine the image enhancement method with the color consistency optimization approach in an inventive way. Consequently, our approach produces aesthetically pleasing images with uniform color tones.

#### IV. CONCLUSION

In response to the problem that various color correction methods neglect to improve image quality while reducing the color difference between images, this article provides a solution for the naturalness restoration and color correction of multiple images with uneven brightness. The proposed method is organized into three primary steps. First, we optimize the luminance components of a single image using adaptive luminance improvement and contrast enhancement methods. The color discrepancies between various luminance components are then eliminated through a color consistency optimization method. Finally, the enhanced images are locally color corrected using multiband blending and block-based *Wallis* transform to remove any visible seams remaining between images.

To evaluate the utility of the suggested approach, we used SAR images spanning the majority of China's land area as study data and juxtaposed our method with two state-of-the-art techniques. Some of the next conclusions can be obtained.

- 1) Qualitative and quantitative analysis of experimental data demonstrates that our method proves to be effective and reliable.
- 2) When juxtaposed with CCGP and CACCC, our strategy lowered indicator CD by about 31.75% and 41.69%, improved metric AG by roughly 109.23% and 69.65%, and increased index PCQI by around 33.79% and 31.90%.
- 3) Experiments reveal that our method exceeds other current methods in terms of reducing color differences across images and recovering image naturalness.

Our method has drawbacks as well. The algorithm proposed in this study is intended to generate high-quality mosaics and fails to consider applying the processing results to quantitative remote sensing, which will serve as the subject of future studies.

#### REFERENCES

- [1] B. Barzycka, M. Błaszczyk, M. Grabiec, and J. Jania, "Glacier facies of Vestfonna (Svalbard) based on SAR images and GPR measurements," *Remote Sens. Environ.*, vol. 221, pp. 373–385, 2019.
- [2] A. Dasgupta, S. Grimaldi, R. Ramsankaran, V. R. Pauwels, and J. P. Walker, "Towards operational SAR-based flood mapping using neuro-fuzzy texture-based approaches," *Remote Sens. Environ.*, vol. 215, pp. 313–329, 2018.
- [3] M. T. Islam and Q. Meng, "An exploratory study of Sentinel-1 SAR for rapid urban flood mapping on Google Earth Engine," *Int. J. Appl. Earth Observ. Geoinf.*, vol. 113, 2022, Art. no. 103002.
- [4] Y. Liu, W. Gong, Y. Xing, X. Hu, and J. Gong, "Estimation of the forest stand mean height and aboveground biomass in Northeast China using SAR Sentinel-1B, multispectral Sentinel-2A, and DEM imagery," *ISPRS-J. Photogramm. Remote Sens.*, vol. 151, pp. 277–289, 2019.
- [5] L. Zhu, J. P. Walker, N. Ye, and C. Rüdiger, "Roughness and vegetation change detection: A pre-processing for soil moisture retrieval from multi-temporal SAR imagery," *Remote Sens. Environ.*, vol. 225, pp. 93–106, 2019.
- [6] G. Zhang et al., "Random cross-observation intensity consistency method for large-scale SAR images mosaics: An example of Gaofen-3 SAR images covering China," *ISPRS-J. Photogramm. Remote Sens.*, vol. 156, pp. 215–234, 2019.
- [7] X. Li, R. Feng, X. Guan, H. Shen, and L. Zhang, "Remote sensing image mosaicking: Achievements and challenges," *IEEE Geosci. Remote Sens. Mag.*, vol. 7, no. 4, pp. 8–22, Dec. 2019.
- [8] S. A. Wegmueller, N. R. Leach, and P. A. Townsend, "LOESS radiometric correction for contiguous scenes (LORACCS): Improving the consistency of radiometry in high-resolution satellite image mosaics," *Int. J. Appl. Earth Observ. Geoinf.*, vol. 97, 2021, Art. no. 102290.
- [9] Y. Li, Y. Li, J. Yao, Y. Gong, and L. Li, "Global color consistency correction for large-scale images in 3-D reconstruction," *IEEE J. Sel. Topics Appl. Earth Observ. Remote Sens.*, vol. 15, pp. 3074–3088, 2022.
- [10] M. Xia, J. Yao, and Z. Gao, "A closed-form solution for multi-view color correction with gradient preservation," *ISPRS-J. Photogramm. Remote Sens.*, vol. 157, pp. 188–200, 2019.
- [11] J. Yang, L. Liu, J. Xu, Y. Wang, and F. Deng, "Efficient global color correction for large-scale multiple-view images in three-dimensional reconstruction," *ISPRS-J. Photogramm. Remote Sens.*, vol. 173, pp. 209–220, 2021.
- [12] W. Ahmad and D. Kim, "Estimation of flow in various sizes of streams using the Sentinel-1 Synthetic Aperture Radar (SAR) data in Han River Basin, Korea," *Int. J. Appl. Earth Observ. Geoinf.*, vol. 83, 2019, Art. no. 101930.
- [13] C. Ding and Z. Ma, "Multi-camera color correction via hybrid histogram matching," *IEEE Trans. Circuits Syst. Video Technol.*, vol. 31, no. 9, pp. 3327–3337, Sep. 2021.
- [14] H. Niu, Q. Lu, and C. Wang, "Color correction based on histogram matching and polynomial regression for image stitching," in *Proc. IEEE 3rd Int. Conf. Image, Vis. Comput.*, 2018, pp. 257–261.
- [15] R. Xie, M. Xia, J. Yao, and L. Li, "Guided color consistency optimization for image mosaicking," *ISPRS-J. Photogramm. Remote Sens.*, vol. 135, pp. 43–59, 2018.
- [16] Z. Hong et al., "Efficient global color, luminance, and contrast consistency optimization for multiple remote sensing images," *IEEE J. Sel. Topics Appl. Earth Observ. Remote Sens.*, vol. 16, pp. 622–637, 2022.
- [17] H. Huang et al., "Deep color calibration for UAV imagery in crop monitoring using semantic style transfer with local to global attention," *Int. J. Appl. Earth Observ. Geoinf.*, vol. 104, 2021, Art. no. 102590.
- [18] J. Liu et al., "Illumination and contrast balancing for remote sensing images," *Remote Sens.*, vol. 6, no. 2, pp. 1102–1123, 2014.
- [19] J. Li, Q. Hu, and M. Ai, "Optimal illumination and color consistency for optical remote-sensing image mosaicking," *IEEE Geosci. Remote Sens. Lett.*, vol. 14, no. 11, pp. 1943–1947, Nov. 2017.
- [20] L. Li, Y. Li, M. Xia, Y. Li, J. Yao, and B. Wang, "Grid model-based global color correction for multiple image mosaicking," *IEEE Geosci. Remote Sens. Lett.*, vol. 18, no. 11, pp. 2006–2010, Nov. 2021.
- [21] M. Oliveira, A. D. Sappa, and V. Santos, "A probabilistic approach for color correction in image mosaicking applications," *IEEE Trans. Image Process.*, vol. 24, no. 2, pp. 508–523, Feb. 2015.
- [22] Y. Zhang, L. Yu, M. Sun, and X. Zhu, "A mixed radiometric normalization method for mosaicking of high-resolution satellite imagery," *IEEE Trans. Geosci. Remote Sens.*, vol. 55, no. 5, pp. 2972–2984, May 2017.
- [23] L. Li, M. Xia, C. Liu, L. Li, H. Wang, and J. Yao, "Jointly optimizing global and local color consistency for multiple image mosaicking," *ISPRS-J. Photogramm. Remote Sens.*, vol. 170, pp. 45–56, 2020.
- [24] L. Yu, Y. Zhang, M. Sun, X. Zhou, and C. Liu, "An auto-adapting global-to-local color balancing method for optical imagery mosaic," *ISPRS-J. Photogramm. Remote Sens.*, vol. 132, pp. 1–19, 2017.
- [25] X. Zhang, R. Feng, X. Li, H. Shen, and Z. Yuan, "Block adjustment-based radiometric normalization by considering global and local differences," *IEEE Geosci. Remote Sens. Lett.*, vol. 19, 2020, Art. no. 8002805.
- [26] M. J. Canty, A. A. Nielsen, and M. Schmidt, "Automatic radiometric normalization of multitemporal satellite imagery," *Remote Sens. Environ.*, vol. 91, no. 3–4, pp. 441–451, 2004.
- [27] G. Wang, X. Huang, Z. Zhou, J. Yang, and T. Jin, "Relative radiometric normalization of SAR images based on bi-direction linear regression model," in *Proc. IEEE RadarCon*, 2011, pp. 333–335.
- [28] O. de Carvalho Jr, R. Guimaraes, R. Gomes, A. de Carvalho, and N. da Silva, "Normalization of multi-temporal images using a new change detection method based on the spectral classifier," in *Proc. IEEE Int. Symp. Geosci. Remote Sens.*, 2006, pp. 771–774.
- [29] S. M. Ya'allah and M. R. Saradjian, "Automatic normalization of satellite images using unchanged pixels within urban areas," *Inf. Fusion*, vol. 6, no. 3, pp. 235–241, 2005.
- [30] M. Hinse, Q. Gwyn, and F. Bonn, "Radiometric correction of C-band imagery for topographic effects in regions of moderate relief," *IEEE Trans. Geosci. Remote Sens.*, vol. 26, no. 2, pp. 122–132, Mar. 1988.
- [31] M. Shimada and T. Ohtaki, "Generating large-scale high-quality SAR mosaic datasets: Application to PALSAR data for global monitoring," *IEEE J. Sel. Topics Appl. Earth Observ. Remote Sens.*, vol. 3, no. 4, pp. 637–656, Dec. 2010.
- [32] M. Shimada and O. Isoguchi, "JERS-1 SAR mosaics of Southeast Asia using calibrated path images," *Int. J. Remote Sens.*, vol. 23, no. 7, pp. 1507–1526, 2002.
- [33] R. Liu, F. Wang, N. Jiao, W. Yu, H. You, and F. Liu, "Radiometric principle-based radiometric normalization method for SAR images Mosaic," *IEEE Geosci. Remote Sens. Lett.*, vol. 19, 2022, Art. no. 4509905.
- [34] T. Shen, J. Wang, T. Fang, S. Zhu, and L. Quan, "Color correction for image-based modeling in the large," in *Proc. Asian Conf. Comput. Vis.*, 2017, pp. 392–407.
- [35] Y. Li, L. Li, J. Yao, M. Xia, and H. Wang, "Contrast-aware color consistency correction for multiple images," *IEEE J. Sel. Topics Appl. Earth Observ. Remote Sens.*, vol. 15, pp. 4941–4955, 2022.
- [36] X. Liu, Q. Xie, Q. Zhao, H. Wang, and D. Meng, "Low-light image enhancement by retinex-based algorithm unrolling and adjustment," *IEEE Trans. Neural Netw. Learn. Syst.*, to be published, doi: [10.1109/TNNLS.2023.3289626](https://doi.org/10.1109/TNNLS.2023.3289626).
- [37] Q. Ma, Y. Wang, and T. Zeng, "Retinex-based variational framework for low-light image enhancement and denoising," *IEEE Trans. Multimedia*, vol. 25, pp. 5580–5588, 2022.

- [38] Y. Qi, C. Liu, H. Wu, X. Shao, and J. Wei, "A multi-layer fusion image enhancement method for visual odometry under poor visibility scenarios," *Int. J. Appl. Earth Observ. Geoinf.*, vol. 115, 2022, Art. no. 103118.
- [39] P. Sidike, V. Sagan, M. Qumsiyeh, M. Maimaitijiang, A. Essa, and V. Asari, "Adaptive trigonometric transformation function with image contrast and color enhancement: Application to unmanned aerial system imagery," *IEEE Geosci. Remote Sens. Lett.*, vol. 15, no. 3, pp. 404–408, Mar. 2018.
- [40] S. Wang, K. Ma, H. Yeganeh, Z. Wang, and W. Lin, "A patch-structure representation method for quality assessment of contrast changed images," *IEEE Signal Process. Lett.*, vol. 22, no. 12, pp. 2387–2390, Dec. 2015.
- [41] Z. Hong et al., "An improved color consistency optimization method based on the reference image contaminated by clouds," *GISci. Remote Sens.*, vol. 60, no. 1, 2023, Art. no. 2259559.



**Changyou Xu** received the B.S. degree in computer science and technology from the School of Modern Economics and Management, Jiangxi University of Finance and Economics, Jiangxi, China, in 2021. He is currently working toward the M.S. degree in computer science and technology with Shanghai Ocean University, Shanghai, China.

His research interests include color correction of remote sensing images.



**Zhonghua Hong** (Member, IEEE) received the Ph.D. degree in geographic information system from Tongji University, Shanghai, China, in 2014.

He has been a Professor with the College of Information Technology, Shanghai Ocean University since 2022. His research interests include satellite/aerial photogrammetry, high-speed videogrammetric, planetary mapping, 3-D emergency mapping, GNSS-R, deep learning, and processing of geospatial Big Data.



**Xiaohua Tong** (Senior Member, IEEE) received the Ph.D. degree in geographic information system from Tongji University, Shanghai, China, in 1999.

From 2001 to 2003, he was a Postdoctoral Researcher with the State Key Laboratory of Information Engineering, Surveying, Mapping, and Remote Sensing, Wuhan University, Wuhan, China. He was a Research Fellow with Hong Kong Polytechnic University, Hong Kong, in 2006, and from 2008 to 2009, he was a Visiting Scholar with the University of California, Santa Barbara, Santa Barbara, CA, USA.

His research interests include photogrammetry and remote sensing, trust in spatial data, and image processing for high-resolution satellite images.



**Shijie Liu** (Member, IEEE) received the Ph.D. degree in cartography and geographic information engineering from Tongji University, Shanghai, China, in 2012.

He is currently a Professor with the College of Surveying and Geo-Informatics, Tongji University, Shanghai, China. His research interests include the geometric exploitation of high-resolution remote sensing and its applications.



**Ruyan Zhou** received the Ph.D. degree in agricultural bio-environment and energy engineering from Henan Agricultural University, Zhengzhou, China, in 2007.

From 2007 to 2008, she was with Zhongyuan University of Technology. She is currently with Shanghai Ocean University, Shanghai, China.



**Haiyan Pan** received the Ph.D. degree in surveying and mapping from Tongji University, Shanghai, China, in 2020.

She is currently a Lecturer with the College of Information Technology, Shanghai Ocean University, Shanghai, China. Her research interests include multitemporal remote sensing data analysis, change detection, and multispectral/hyperspectral image classification.



**Yun Zhang** received the Ph.D. degree in applied marine environmental studies from Tokyo University of Maritime Science and Technology, Tokyo, Japan, in 2008.

Since 2011, he has been a Professor with the College of Information and Technology, Shanghai Ocean University, Shanghai, China. His research interests include the study of navigation system reflection signal technique and its maritime application.



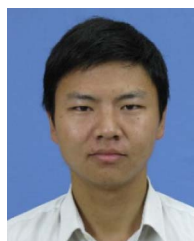
**Yanling Han** received the B.E. degree in mechanical design and manufacturing and the M.E. degree in mechanical automation from Sichuan University, Sichuan, China, in 1996 and 1999, respectively, and the Ph.D. degree in engineering and control theory from Shanghai University, Shanghai, China, in 2005.

She is currently a Professor with Shanghai Ocean University, Shanghai, China. Her research interests include the study of ocean remote sensing, flexible system modeling, and deep learning.



**Jing Wang** received the Ph.D. degree in biomedical engineering from the Department of Biomedical Engineering, Shanghai Jiaotong University, Shanghai, China, in 2014.

Since 2015, she has been a Lecturer with the College of Information Technology, Shanghai Ocean University, Shanghai, China. Her research interests include computer vision and medical image processing.



**Shuhu Yang** received the Ph.D. degree in physics from the School of Physics, Nanjing University, Nanjing, China, in 2012.

Since 2012, he has been a Lecturer with the College of Information Technology, Shanghai Ocean University, Shanghai, China. His research interests include the evolution of the Antarctic ice sheet, hyperspectral remote sensing, and the use of navigational satellite reflections.